# Towards Room-Temperature Exciton–Polariton Supersolidity Driven by Guided Optical Parametric Oscillation

Lingyu Tian(田玲钰)[1], Yusong Gan(甘雨松)[2], Ying Shi(石莹)[2], Luobing Xu(许洛冰)[2], Huawen Xu(许华文)[1*], and Qihua Xiong(熊启华)[2,1,3*]

[1]*Beijing Academy of Quantum Information Sciences, Beijing 100193, China*
[2]*State Key Laboratory of Low-Dimensional Quantum Physics and Department of Physics, Tsinghua University, Beijing 100084, China*
[3]*Frontier Science Center for Quantum Information, Beijing 100084, China*

(Received 2 August 2025; accepted manuscript online 25 August 2025)

Supersolidity is a counterintuitive quantum phase of matter where the long-range spatial order of a solid coexists with the frictionless flow characteristic of a superfluid. Recently, evidence of supersolidity has been demonstrated in polariton condensates in III-V photonic crystal microcavities by condensing into a topological bound state in the continuum, offering a new light–matter hybrid platform for exploring such quantum phase. In this work, we propose a theoretical scheme for realizing room-temperature supersolidity based on halide perovskite exciton polaritons operating in the optical parametric oscillation regime. By employing a waveguide microcavity geometry, we confine polariton scattering direction in reciprocal space, enabling controlled momentum selection. Leveraging the intrinsic nonlinear interactions among polaritons, we theoretically demonstrate the spontaneous breaking of both continuous translational symmetry and global phase symmetry, i.e., the evidence of supersolidity. Furthermore, we identify a tunable phase transition sequence in our system: from a Bose–Einstein condensate to a supersolid phase, and ultimately to an insulating phase, as the nonlinear interaction strength increases.

DOI: 10.1088/0256-307X/42/9/090405 CSTR: 32039.14.0256-307X.42.9.090405

*1. Introduction.* A supersolid is a unique phase of matter that simultaneously exhibits the characteristic properties of both a solid and a superfluid.[1] It combines two seemingly contradictory orders as crystalline and superfluid order, which respectively break translational symmetry and global U(1) gauge symmetry. In the supersolid phase (SSP), the excitation spectrum is significantly enriched by the interplay of spatial modulation and long-range phase coherence.[2] The gapless Goldstone mode, which is different from the conventional one associated with global phase fluctuations, reflects the rigidity of the periodic density modulation.[3] Also, a gapped Higgs mode could be present with amplitude oscillations of the modulation.[4]

Supersolidity was first proposed in the 1970s in the context of helium-4.[5,6] Over the past decade, compelling experimental evidence for SSPs has been obtained in ultracold atomic Bose–Einstein condensates (BECs),[7–12] marking a significant milestone in the study of quantum matter. However, these realizations remain largely confined to ultracold atomic systems, which require stringent cryogenic conditions. Moreover, achieving and maintaining coherence in such systems is inherently challenging. Very recently, both theoretical[13] and experimental works[14] have demonstrated that light can acquire supersolid properties when strongly coupled to matter in the form of microcavity exciton polaritons. This realization of a photonic supersolid represents a major advancement, opening new directions for exploring the underlying physics of supersolidity in driven-dissipative, room-temperature platforms.

Microcavity exciton polaritons, formed by the strong coupling between cavity photons and quantum well excitons, inherit hybrid properties from both constituents.[15,16] They simultaneously exhibit an extremely low effective mass (arising from their photonic component) and strong nonlinear interactions (originating from the excitonic component), making them ideal for applications in nonlinear photonics and a promising platform for studying quantum fluid behaviors, such as nonlinear optical devices,[17,18] topological lasers,[19–22] exciton polariton condensation,[20,23–25] and superfluidity.[26] Recent studies have demonstrated the possibility of realizing a supersolid state in exciton polariton system based on bound states in the continuum formed in GaAs-based microcavities under cryogenic conditions.[14] However, current designs heavily rely on precisely etched grating structures on top of the distributed Bragg reflectors (DBRs), requiring subwavelength fabrication precision. By contrast, halide perovskite microcavities have been shown to support exciton polariton condensation[20,24] and quantum fluid behaviors[26] at room temperature, offering a promising and experimentally accessible platform for studying exotic quantum phases even at room temperature.

*Corresponding authors. Email: xuhw@baqis.ac.cn; qihua_xiong@tsinghua.edu.cn
© 2025 Chinese Physical Society and IOP Publishing Ltd. All rights, including for text and data mining, AI training, and similar technologies, are reserved.

In this Letter, we propose a theoretical scheme for realizing the observation of polariton supersolidity in a planar waveguide microcavity operating in the optical parametric oscillation (OPO) regime. By confining polariton scattering in momentum space, engineering the excitation conditions, and exploiting the intrinsic nonlinearity of the system, we induce the spontaneous breaking of both continuous translational symmetry and global phase symmetry—hallmarks of a SSP. Through numerical calculations of the first-order spatial coherence function $g^{(1)}$, we find that as the nonlinear interaction strength increases, the system undergoes a transition from a BEC to a supersolid, and finally to an insulating phase (IP). In both the BEC and SSP, the system maintains global phase coherence, characterized by a coherence length larger than the pumped excitation region; in contrast, the IP exhibits only local coherence, with a coherence length smaller than the pumped region.

*2. Theoretical Model.* The schematic of our considered model is demonstrated in Fig. 1(a), where the halide perovskite gain materials are embedded between DBRs, enabling the formation of exciton polaritons through strong exciton–photon coupling. The structure is extended along $x$-direction to form a quasi-one-dimensional geometry. Moreover, in our system, two distinct lower polariton (LP) branches with different energies coexist, which can be experimentally realized in perovskite microcavities by tailoring the thickness of the microcavity.[27,28] In this case, resonantly exciting the bottom of the higher-energy LP branch can lead to the onset of OPO due to nonlinear interactions, as shown in Fig. 1(b). This mechanism enables energy-degenerate scattering into signal/idler states at opposite finite momentum.

The polariton OPO process can be characterized by the driven-dissipative Gross–Pitaevskii equation under mean-field approximation (the derivation details are given in the Supplementary Materials):

$$\mathrm{i}\hbar\dot{\psi}(\boldsymbol{r},t) = \left[(E - \mathrm{i}\gamma/2) + \alpha|\psi(\boldsymbol{r},t)|^2\right]\psi(\boldsymbol{r},t) + P(\boldsymbol{r})\,, \quad (1)$$

where $\psi(\boldsymbol{r},t)$ denotes the polariton wave function at position $\boldsymbol{r}$ and time $t$. $\gamma$ is the decay rate, inversely related to the polariton lifetime. $\alpha$ characterizes the nonlinear interaction strength. The kinetic term can be expressed as $E = (E_p(\boldsymbol{k}) + E_x)/2 - \sqrt{\Omega^2 + [E_p(\boldsymbol{k}) - E_x]^2}/2 - \Delta E$, where $E_p(\boldsymbol{k}) = \hbar^2\boldsymbol{k}^2/(2m_p)$ is the cavity photon dispersion, $E_x$ is the exciton energy, and $\Omega$ is the Rabi splitting. Here, we consider $\Omega = 120\,\mathrm{meV}$, which is related to the perovskite microcavities.[20] $\Delta E$ denotes the detuning between two different LP branches. The resonant excitation applied to the microcavity at normal incidence is represented by $P(\boldsymbol{r})$, given by $P(\boldsymbol{r}) = P_0 \mathrm{e}^{-(x^2/\sigma_x^2 + y^2/\sigma_y^2)}$.

The physical process of exciton polariton OPO is typically identified by analyzing the intensity and energy spectrum of the emitted photons, with the latter typically obtained from energy–momentum-resolved measurements.

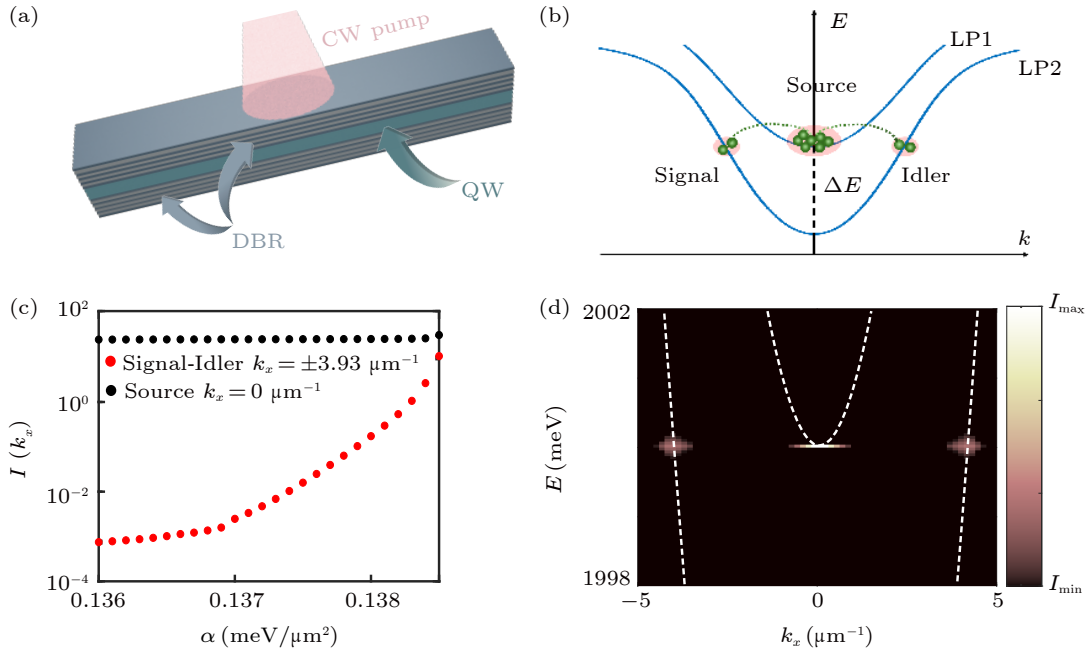


**Fig. 1.** (a) Sketch of the proposed setup. A planar microcavity is resonantly excited by a CW pump at normal incidence $\boldsymbol{k} = (k_x, k_y) = 0$. The pump spot extends along the $y$ direction to ensure spatial uniformity in that direction. The quantum wells (QWs) in our system are based on halide perovskites, which serve as the active gain medium. (b) Schematic illstration of the energy-degenerate OPO in the microcavity. Stimulated by a scattering process originating from a condensate in one polariton branch, correlated polariton pairs emerge at high-$k$ states in the adjacent dispersion branch. $\Delta E$ is the detuning between two different LP branches at $\boldsymbol{k} = 0$. (c) Steady state momentum distributions for condensation and signal-idler modes as functions of nonlinear interaction strength. (d) Energy–momentum-resolved emission intensity $I(E, k_x)$ under $\alpha = 0.138\,\mathrm{meV/\mu m^2}$. Throughout this study, we fix $\gamma = 0.25\,\mathrm{meV}$ (corresponding lifetime is about 3 ps, pump width $\sigma_x = 8\,\mu\mathrm{m}$, $\sigma_y = 4\,\mu\mathrm{m}$ and $\Delta E = 16\,\mathrm{meV}$.)

Therefore, we calculate the steady-state momentum distribution through the Fourier transform of the wavefunction at time $t$,

$$I(k_x, k_y) = \left| \iint \psi(x, y)\, \mathrm{e}^{-\mathrm{i}(k_x x + k_y y)} \mathrm{d}x\mathrm{d}y \right|^2 . \tag{2}$$

We extract the polariton intensity at zero and finite momentum as functions of the nonlinear interaction strength $\alpha$, as shown in Fig. 1(c). Due to the resonant excitation at zero momentum, the polariton intensity at $k_x = 0$ remains high and exhibits minimal variation with increasing nonlinear interaction strength. In contrast, the intensity at finite momentum increases significantly once the interaction exceeds a critical value (in our case, $\alpha \approx 0.137\,\mathrm{meV}/\mu\mathrm{m}^2$) and eventually becomes comparable to that at $k_x = 0$, indicating the onset of multimode occupation driven by nonlinear scattering effects. The corresponding dispersion results are shown in Fig. 1(d), where the peak at $k_x = 0$ is related to the polariton condensate and the two peaks at $\tilde{k}_x = \pm 3.93\,\mu\mathrm{m}^{-1}$ are a distinctive feature of the nonlinear scattering from the condensate into signal/idler states.

*3. Phase Transition.* While the signal state at $\boldsymbol{k} = 0$ remains stabilized by resonant excitation, increasing the nonlinear interaction strength introduces significant modifications to the collective behavior of the polariton system. Beyond a critical threshold, the interplay between nonlinearity, coherence, and parametric scattering gives rise to emergent many-body phases. In what follows, we demonstrate that by tuning the interaction strength within the OPO regime, the polariton system undergoes a sequence of phase transitions, i.e., from a BEC to a SSP, and eventually to an IP, as shown in Fig. 2(a), highlighting the potential of OPO-driven polaritons as a platform for exploring exotic quantum phases. To illustrate these transitions, we first analyze the evolution of the density distribution $I(\boldsymbol{r}) = |\psi(\boldsymbol{r})|^2$ at different values of $\alpha$, as shown in Figs. 2(b)–2(d). Owing to the translational invariance along the $y$-direction, only the $x$-axis is shown. The first phase emerges at relatively small values of $\alpha$, corresponds to a conventional BEC regime where OPO has not yet been triggered. The density profile remains unmodulated and retains the Gaussian shape of the pump, see Fig. 2(b) and the region denoted BEC in Fig. 2(a). As $\alpha$ increases to the threshold where OPO occurs, the system enters the second stage, which is characterized by the appearance of periodic density modulation in real space. The density profile develops multiple local maxima that form a regular spatial pattern with partial overlap, see Fig. 2(c). This spatial modulation allows coherent tunneling of particles between modes, leading to the establishment of global phase coherence across the system, later quantified by the link strength $S$. Such a phase, in which the coexistence of long-range phase coherence and periodic density modulation, is identified as SSP, as shown in the region in Fig. 2(a). When further increasing $\alpha$, the density overlap rapidly decreases and eventually vanishes, see Fig. 2(d).

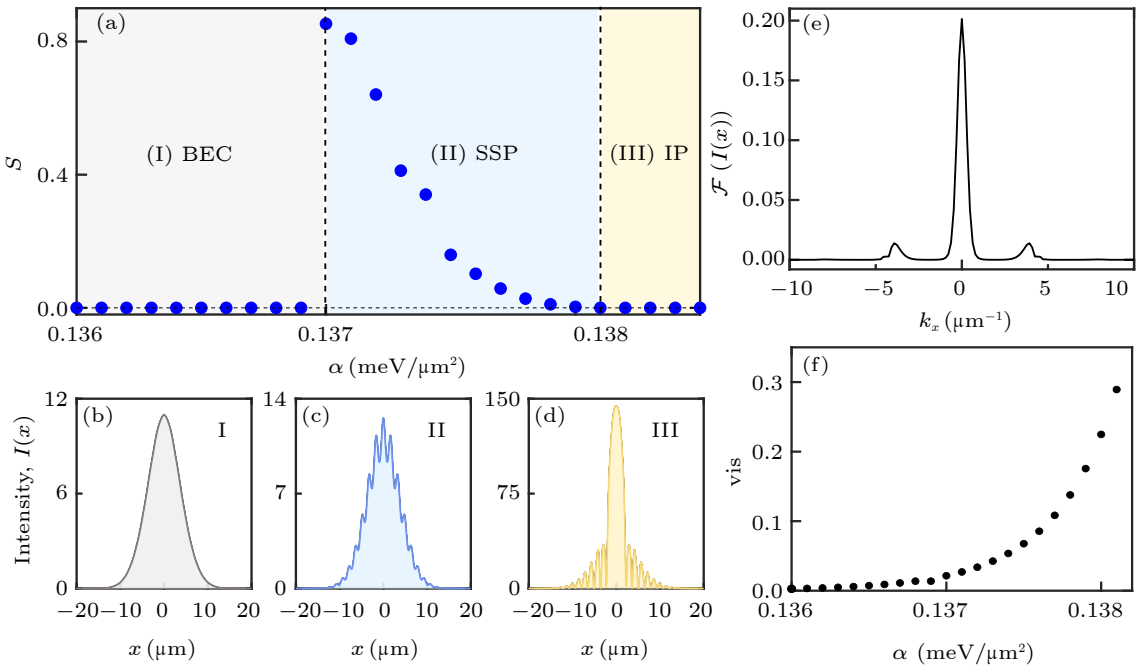


**Fig. 2.** (a) Phase transistion induced by nonlinear interaction strength, characterized by the link strength $S$. The blue dots show the trend of $S$ values between different phases. The gray region identifies BEC phase, featuring a single broad Gaussian peak in the density profile $I(x)$, as exemplified in (b). The light blue region identifies the SSP, featuring by clear density modulation, as shown in (c). The light yellow region identifies the IP, which exhibits density modulation without global phase coherence, as shown in (d). (b)–(d) show real space intensity distribution at $\alpha = 0.1365$, 0.1377, and $0.1385\,\mathrm{meV}/\mu\mathrm{m}^2$. We mainly focus on the density distribution within the pumped excitation region, $x \in [-4, 4]$ μm. (e) Spectral components, associated to steady-state modulation profiles, as a function of $k_x$. Peaks at finite momentum reveal the emergence of a density modulation. Here, we consider $\alpha = 0.1377\,\mathrm{meV}/\mu\mathrm{m}^2$. (f) The modulation amplitude is quantified by the visibility, vis, defined as the ratio of the peak intensity at finite momentum to that at zero momentum.

As a result, inter-mode tunneling is suppressed, leading to a complete breakdown of global phase coherence. We identify this third phase as an insulating phase (IP), analogous to the 'insulating droplet array' known from cold atom systems, see the IP region in Fig. 2(a).

To investigate the supersolid nature of the density-modulated phase and to distinguish it from the insulating regime, we quantitatively calculate the wavefunction overlap $S$, a quantity introduced to characterize the tunneling rate between droplets.[10] Within the Josephson-junction picture,[29,30] the tunneling rate of atoms between neighboring droplets is governed by the wavefunction overlap. The single-particle tunneling rate can be estimated under a Gaussian approximation,[31] where the insulating droplet phase corresponds to extremely small values of $S$, indicating tunneling timescales that extremely exceed any other relevant timescales. In contrast, the SSP exhibits a substantial value of $S$, corresponding to shorter tunneling times. Hence, $S$ provides a quantitative measure of the system's ability to establish and maintain global phase coherence. To extract $S$ in our system, we fit the real space intensity profile $I(x)$ of each density peak with a Gaussian function. For two neighboring localized maxima separated by a distance $d_n$ and having the same Guaasian width $w_n$, $S$ is simply $S = 1/n \sum_n \exp(-d_n^2/4w_n^2)$. Here, $n$ denotes the number of pairs of peaks at the center of the spectrum. Considering the dominant contribution of the density peaks and pump spot size, we set $n = 2$ in our calculation. As shown in Fig. 2(a), in the BEC regime, where no density modulation is present, $S$ is set to zero. At the transition from BEC to SSP, i.e., at $\alpha = 0.137\,\mathrm{meV}/\mu\mathrm{m}^2$, a density modulation emerges, and the overlap $S$ reaches its maximum value when the modulation amplitude is minimal. With further increase in $\alpha$, the overlap $S$ gradually decreases, indicating a progressive reduction in the tunneling rate between modes. The behavior of the gradual decrease in $S$ also suggests that the transition from SSP to IP has a smooth characteristic in nature. This evolution is qualitatively consistent with the density profiles presented in Figs. 2(b)–2(d) discussed previously.

*4. Density Modulation and Phase Coherence.* We now focus on the evolution of density modulation and phase coherence across the BEC–SSP–IP transition. Firstly, to further analyze the spatial characteristics of density modulation in the SSP, we perform a Fourier transform of the real space intensity distribution to extract its spectral components in momentum space. In this way, information can be obtained regarding the presence of periodic structures in the system and its corresponding spatial frequency. In Fig. 2(e), we present the Fourier results with $\alpha = 0.1377\,\mathrm{meV}/\mu\mathrm{m}^2$. The spectrum appears strongly peaked not only at zero momentum, but also around $\tilde{k}_x \approx \pm 3.93\,\mu\mathrm{m}^{-1}$, corresponding to the overall average density component and the emergence of a modulated structure induced by the interactions between the source and signal/idler states. This agrees well with the emission spectrum shown in Fig. 1(d). Notably, the spatial periodicity estimated by $2\pi/\tilde{k}_x \approx 1.6\,\mu\mathrm{m}$ is also in good agreement with the real space modulation shown in Fig. 2(c). To quantify the

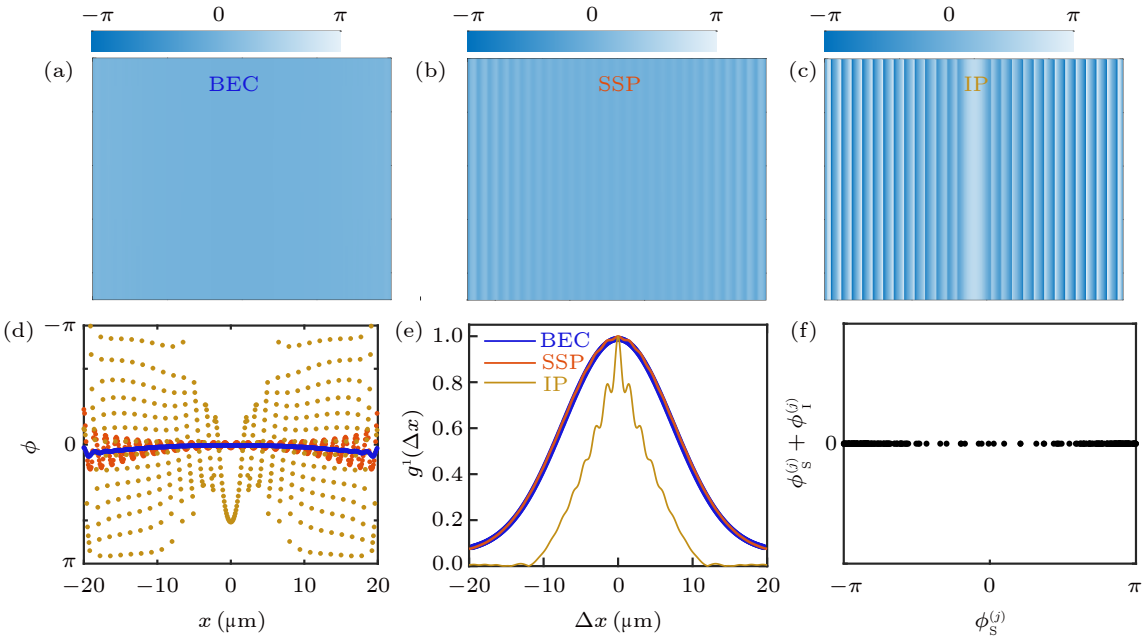


**Fig. 3.** (a)–(c) Phase maps $\phi(x, y)$ provide phase distribution in the different phases: (a) $\phi(x, y) = 0$ for BEC phase, (b) $\phi(x, y)$ normally distributed around 0 with $0.07\pi$ standard deviation for SSP, and (c) $\phi(x, y)$ uniformly distributed between $[-\pi, \pi]$ for IP. (d) The phase distribution $\phi$ along the $x$-direction at a fixed $y$ position, obtained from (a)–(c). The colors correspond to the phase markings in the phase maps. (e) First-order spatial coherence $g^1(\Delta x)$ for different phases, showing the transition from global phase coherence to local phase coherence. (f) The sum of signal–idler phases $\left(\phi_{\mathrm{S}}^{(j)} + \phi_{\mathrm{I}}^{(j)}\right)$ as a function of the signal phase $\phi_{\mathrm{S}}^{(j)}$ for each independent simulation $j$, which illustrates the spontaneous phase symmetry breaking characteristic of the SSP. Here, we consider $\alpha = 0.1365$, 0.1377, and $0.1385\,\mathrm{meV}/\mu\mathrm{m}^2$, corresponding to the BEC, supersolid, and IP, respectively.

degree of density modulation, we introduce the visibility parameter vis $= 2 * \mathcal{F}(I(x))_{\tilde{k}_x}/\mathcal{F}(I(x))_{k_x=0}$. As shown in Fig. 2(f), the modulation strength increases from $\alpha = 0.137\,\mathrm{meV}/\mu\mathrm{m}^2$, which is consistent with the results obtained from the $S$. It is worth emphasizing that, in the IP, the spectral peaks are not limited to $\tilde{k}_x$, but are instead distributed over multiple $k_x$ components, indicating that the increased nonlinearity leads to more complex scattering processes among the modes.[32]

With increasing nonlinear interaction strength, the phase distributions differ noticeably among the BEC, SSP and IP, as illustrated in Figs. 3(a)–3(c). Figure 3(d) presents the phase profiles along the $x$-direction at a fixed $y$ value for the three phases, with colors matching those in the phase map. To further quantify their coherence properties, we evaluate the first-order coherence function, which is defined as[33,34]

$$g^1(\Delta x) = \frac{\langle \psi^*(x,y)\psi(x+\Delta x,y)\rangle_N}{\sqrt{\langle|\psi(x,y)|^2\rangle_N \langle|\psi(x+\Delta x,y)|^2\rangle_N}}, \quad (3)$$

which measures the degree of phase correlation between a distance $\Delta x$. Here, $\langle\rangle_N$ represents an average over $N = 50$ independent simulation runs. To this end, random noise $\xi(\boldsymbol{r})$ is included in our considered model. Figure 3(e) shows the increase with $\alpha$ of $g^1(\Delta x)$. It can be seen that with increasing $\alpha$, the long distance behavior of $g^1$ gradually decays to zero, reflecting the disappearance of long-range phase coherence. By fitting $g^1(\Delta x) = \mathrm{e}^{-|\Delta x|/\ell_c}$, the coherence length $\ell_c$ can be extracted. When $\ell_c$ exceeds or is comparable to the system size defined by the pump spot size, the system exhibits long-range phase coherence; otherwise, only local coherence is present.[35,36] Therefore, comparing coherence length with the pump size provides a quantitative criterion for distinguishing the SSP from the IP. Under this criterion, we observe a transition from global phase coherence in the BEC and SSP to local phase coherence in the IP, where $\ell_c \approx 6.5 > 4\,\mu\mathrm{m}$ is reduced to $\ell_c \approx 2.7 < 4\,\mu\mathrm{m}$. The intensity modulation of the coherence function is in phase with the density modulation, specifically, regions with smaller coherence coincide with the low-density regions of the polariton condensate. This behavior confirms the loss of global spatial coherence, which coincides with the continuous decrease of the link strength $S$ toward zero.

Although the amplitude and phase of the source mode are fully determined by the laser, the phases of the signal/idler modes remain undetermined in the OPO regime. This phase freedom stems from the invariance of the equations of motion under equal and opposite phase rotations of the signal-idler modes,[37] namely

$$\psi_S \to \psi_S \mathrm{e}^{\mathrm{i}\phi_S}, \quad \psi_I \to \psi_I \mathrm{e}^{\mathrm{i}\phi_I}, \quad (4)$$

which preserves the parametric coupling condition. Therefore, the OPO state exhibits spontaneous breaking of U(1) phase-rotation symmetry: in each random realization, the phase $\phi_S$ ($\phi_I$) is randomly selected within the range $[-\pi, \pi]$. The sum of the phase of signal–idlers states ($\phi_S + \phi_I$) remains zero, consistent with momentum conservation in the OPO process. To verify this spontaneous phase selection numerically, we perform 300 independent simulations at $\alpha = 0.1377\,\mathrm{meV}/\mu\mathrm{m}^2$, which lies within the SSP. In each realization $j$, the signal/idler phases $\phi_S^{(j)}$ ($\phi_I^{(j)}$) are extracted from $\tilde{k}_x = \pm 3.93\,\mu\mathrm{m}^{-1}$ [see Fig. 2(e)]. The numerical results, displayed in Fig. 3(f), reveal that $\phi_S$ takes randomly spanning the range $[-\pi, \pi]$ and satisfies $\phi_S^{(j)} + \phi_I^{(j)} = 0$. The resulting spontaneous breaking of a phase symmetry in real space serves as clear evidence for an exciton polariton SSP, whose spatial modulation behaves as $\cos(\tilde{k}_x\, x + \phi_S^{(j)})$.

*5. Non-Rigidity of the Modulation.* The periodicity of the density modulation observed in the SSP is determined by the wavevector difference between the source and the signal/idler modes. Since the OPO process conserves energy, the momenta of the signal and idler states are constrained by the energy of the source mode, i.e., the condensation energy. As the source energy shifts along the parabolic dispersion, the signal and idler wavevectors adjust accordingly to satisfy both energy and momentum conservation. In Fig. 4, we increase the detuning between two LP branches to $\Delta E = 25\,\mathrm{meV}$ to investigate the evolution of the modulation and evaluate its influence on the modulation periodicity. We find that the signal/idler wavevectors shift outward to around $\tilde{k}_x = \pm 5.18\,\mu\mathrm{m}^{-1}$, leading to a reduced modulation period of approximately $1.2\,\mu\mathrm{m}$. These results clearly demonstrate the non-rigid nature of the SSP, which exhibits tunable behavior reminiscent of roton-like excitations, and further confirm the

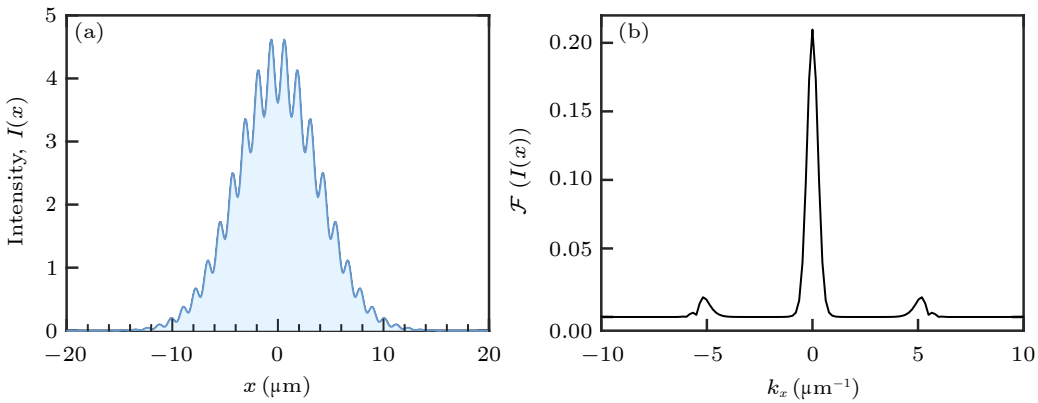


**Fig. 4.** Nonrigidity of exciton polariton supersolids. (a) The density distribution $I(x)$ and spectral components for $\alpha = 0.374\,\mathrm{meV}/\mu\mathrm{m}^2$ and detuning $\Delta E = 25\,\mathrm{meV}$.

spontaneous breaking of continuous symmetry in the system.

*6. Discussion and Conclusions.* To clarify the mechanism behind the reduced spatial coherence at high OPO strength, we point out that this effect cannot be explained by a simple interference of three mutually coherent beams (signal, idler, and pump), where mutual coherence would remain unchanged. In the polariton OPO process, the signal and idler modes are generated through nonlinear parametric scattering, creating correlated photon pairs rather than independent coherent waves. This pair generation leads to multimode occupation in momentum space, introducing relative phase fluctuations that degrade the first-order spatial coherence.[38] These effects are inherently captured in the Gross–Pitaevskii model through nonlinear interactions and multimode coupling.

In summary, our theoretical results uncover a route to achieving room temperature polariton supersolidity in planar microcavities, offering a new framework for engineering exotic quantum phases in driven-dissipative systems. By imposing directional constraints in reciprocal space through a waveguide geometry and exploiting the nonlinear scattering inherent to exciton polaritons, our numerical simulations show that both translational and phase symmetries can be spontaneously broken within the OPO regime. This interplay of symmetry breaking in a non-equilibrium setting leads to a controllable and tunable SSP, marking a significant step beyond equilibrium condensate physics. Notably, the observed transition sequence—from a BEC-like fluid to a supersolid, and ultimately to an interaction-induced insulating state—highlights the versatility of polariton systems as quantum simulators of collective behavior. These findings not only enrich the fundamental understanding of supersolidity in photonic platforms, but also pave the way for realizing reconfigurable, low-power quantum fluid circuits and optically controlled synthetic matter with programmable order. Our approach is designed using parameters consistent with perovskite microcavities, thus, it holds strong potential for realizing room temperature supersolidity in experiments.

It is also worth emphasizing that, in addition to the perovskite system, two-dimensional materials may also host a SSP within our theoretical framework. For example, theoretical studies have predicted that in transition metal dichalcogenide monolayers, an in-plane magnetic field can induce exciton Bose–Einstein condensation,[39] and an electric field can drive the formation of exciton vortices.[40] These findings indicate the potential for realizing superfluidity in two-dimensional material platforms. The Rashba spin–orbit coupling, induced by a perpendicular electric field, can introduce finite-momentum condensation, analogous to that induced by OPO process, opens a promising pathway towards the potential realization of a SSP in such systems.

*Acknowledgments.* This work was supported by the National Natural Science Foundation of China (Grant No. 12434011 obtained by Q X) and the China Postdoctoral Science Foundation (Grant No. Y24PJ2425214 obtained by L T). The authors acknowledge helpful discussions with Daniele Sanvitto and Dario Gerace. Q X acknowledges the support from the State Key Laboratory of Low-Dimensional Quantum Physics at Tsinghua University.

# References

[1] Boninsegni M and Prokof'Ev N V 2012 *Rev. Mod. Phys.* **84** 759
[2] Guo M Y, Böttcher F, Hertkorn J, Schmidt J N, Wenzel M, Büchler H P, Langen T, and Pfau T 2019 *Nature* **574** 386
[3] Saccani S, Moroni S, and Boninsegni M 2012 *Phys. Rev. Lett.* **108** 175301
[4] Léonard J, Morales A, Zupancic P, Donner T, and Esslinger T 2017 *Science* **358** 1415
[5] Kuklov A B, Pollet L, Prokof'ev N V, and Svistunov B V 2014 *Phys. Rev. B* **90** 184508
[6] Kim E and Chan M H W 2004 *Nature* **427** 225
[7] Léonard J, Morales A, Zupancic P, Esslinger T, and Donner T 2017 *Nature* **543** 87
[8] Li J R, Lee J, Huang W J, Burchesky S, Shteynas B, Top F, Jamison A O, and Ketterle W 2017 *Nature* **543** 91
[9] Böttcher F, Schmidt J N, Wenzel M, Hertkorn J, Guo M Y, Langen T, and Pfau T 2019 *Phys. Rev. X* **9** 011051
[10] Chomaz L, Petter D, Ilzhöfer P, Natale G, Trautmann A, Politi C, Durastante G, van Bijnen R M W, Patscheider A, Sohmen M, Mark M J, and Ferlaino F 2019 *Phys. Rev. X* **9** 021012
[11] Tanzi L, Lucioni E, Famà F, Catani J, Fioretti A, Gabbanini C, Bisset R. N, Santos L, and Modugno G 2019 *Phys. Rev. Lett.* **122** 130405
[12] Ilzhöfer P, Sohmen M, Durastante G, Politi C, Trautmann A, Natale G, Morpurgo G, Giamarchi T, Chomaz L, Mark M J, and Ferlaino F 2021 *Nat. Phys.* **17** 356
[13] Nigro D, Trypogeorgos D, Gianfrate A, Sanvitto D, Carusotto I, and Gerace D 2025 *Phys. Rev. Lett.* **134** 056002
[14] Trypogeorgos D, Gianfrate A, Landini M, Nigro D, Gerace D, Carusotto I, Riminucci F, Baldwin K W, Pfeiffer L N, Martone G I, De Giorgi M, Ballarini D, and Sanvitto D 2025 *Nature* **639** 337
[15] Carusotto I and Ciuti C 2013 *Rev. Mod. Phys.* **85** 299
[16] Byrnes T, Kim N Y, and Yamamoto Y 2014 *Nat. Phys.* **10** 803
[17] Sanvitto D and Kéna-Cohen S 2016 *Nat. Mater.* **15** 1061
[18] Li H, Chen F, Jia H Y, Ye Z Y, Zhou H, Luo S, Shi J H, Sun Z R, Xu H L, Xu H X, Byrnes T, Chen Z H, and Wu J 2024 *Nat. Photonics* **18** 864
[19] Klembt S, Harder T H, Egorov O A, Winkler K, Ge R, Bandres M A, Emmerling M, Worschech L, Liew T C H, Segev M, Schneider C, and Höfling S 2018 *Nature* **562** 552
[20] Su R, Ghosh S, Wang J, Liu S, Diederichs C, Liew T C H, and Xiong Q H 2020 *Nat. Phys.* **16** 301
[21] Wu J Q, Ghosh S, Gan Y S, Shi Y, Mandal S, Sun H D, Zhang B, Liew T C H, Su R, and Xiong Q H 2023 *Sci. Adv.* **9** eadg4322
[22] Su R, Ghosh S, Liew T C H, and Xiong Q H 2021 *Sci. Adv.* **7** eabf8049
[23] Deng H, Haug H, and Yamamoto Y 2010 *Rev. Mod. Phys.* **82** 1489
[24] Su R, Diederichs C, Wang J, Liew T C H, Zhao J X, Liu S, Xu W G, Chen Z H, and Xiong Q H 2017 *Nano Lett.* **17** 3982
[25] Ghosh S, Su R, Zhao J X, Fieramosca A, Wu J Q, Li T F, Zhang Q, Li F, Chen Z H, Liew T, Sanvitto D, and Xiong Q H 2022 *Photonics Insights* **1** R04

[26] Peng K, Tao R J, Haeberlé L, Li Q W, Jin D F, Fleming G R, Kéna-Cohen S, Zhang X, and Bao W 2022 *Nat. Commun.* **13** 7388
[27] Wu J Q, Ghosh S, Su R, Fieramosca A, Liew T C H, and Xiong Q H 2021 *Nano Lett.* **21** 3120
[28] Wu J Q, Su R, Fieramosca A, Ghosh S, Zhao J X, Liew T C H, and Xiong Q H 2021 *Adv. Photonics* **3** 055003
[29] Javanainen J 1986 *Phys. Rev. Lett.* **57** 3164
[30] Raghavan S, Smerzi A, Fantoni S, and Shenoy S R 1999 *Phys. Rev. A* **59** 620
[31] Wenzel M, Böttcher F, Schmidt J N, Eisenmann M, Langen T, Pfau T, and Ferrier-Barbut I 2018 *Phys. Rev. Lett.* **121** 030401
[32] Dunnett K, Ferrier A, Zamora A, Dagvadorj G, and Szymańska M H 2018 *Phys. Rev. B* **98** 165307
[33] Dagvadorj G, Fellows J M, Matyjaśkiewicz S, Marchetti F M, Carusotto I, and Szymańska M H 2015 *Phys. Rev. X* **5** 041028
[34] Bao R Q, Xu H W, Verstraelen W, and Liew T C H 2023 *Phys. Rev. B* **108** 235305
[35] Daskalakis K S, Maier S A, and Kéna-Cohen S 2015 *Phys. Rev. Lett.* **115** 035301
[36] Deng H, Weihs G, Snoke D, Bloch J, and Yamamoto Y 2003 *Proc. Natl. Acad. Sci.* **100** 15318
[37] Wouters M and Carusotto I 2007 *Phys. Rev. A* **76** 043807
[38] Wouters M and Carusotto I 2006 *Phys. Rev. B* **74** 245316
[39] Wang D F, Chen Y D, Niu Z C, Lou W K, and Chang K 2024 *Chin. Phys. Lett.* **41** 087101
[40] Chen Y D, Huang Y W, Lou W K, Cai Y Y, and Chang K 2020 *Phys. Rev. B* **102** 165413